



Mechanical power from thermocapillarity on superhydrophobic surfaces

Michael D. Mayer¹ , Toby L. Kirk¹ , Marc Hodes² and Darren Crowdy¹ 

¹Department of Mathematics, Imperial College London, Exhibition Road, London SW7 2AZ, UK

²Department of Mechanical Engineering, Tufts University, Robinson Hall, Medford, MA 02155, USA

Corresponding author: Michael D. Mayer, m.mayer@imperial.ac.uk

(Received 27 June 2024; revised 2 January 2025; accepted 4 January 2025)

Crowdy *et al.* (2023 *Phys. Rev. Fluids*, vol. 8, 094201), recently showed that liquid suspended in the Cassie state over an asymmetrically spaced periodic array of alternating cold and hot ridges such that the menisci spanning the ridges are of unequal length will be pumped in the direction of the thermocapillary stress along the longer menisci. Their solution, applicable in the Stokes flow limit for a vanishingly small thermal Péclet number, provides the steady-state temperature and velocity fields in a semi-infinite domain above the superhydrophobic surface, including the uniform far-field velocity, i.e. pumping speed, the key engineering parameter. Here, a related problem in a finite domain is considered where, opposing the superhydrophobic surface, a flow of liquid through a microchannel is bounded by a horizontally mobile smooth wall of finite mass subjected to an external load. A key assumption underlying the analysis is that, on a unit area basis, the mass of the liquid is small compared with that of the wall. Thus, as shown, rather than the heat equation and the transient Stokes equations governing the temperature and flow fields, respectively, they are quasi-steady and, as a result, governed by the Laplace and Stokes equations, respectively. Under the further assumption that the ridge period is small compared with the height of the microchannel, these equations are resolved using matched asymptotic expansions which yield solutions with exponentially small asymptotic errors. Consequently, the transient problem of determining the velocity of the smooth wall is reduced to an ordinary differential equation. This approach is used to provide a theoretical demonstration of the conversion of thermal energy to mechanical work via the thermocapillary stresses along the menisci.

Key words: microfluidics, microscale transport, thermocapillarity

1. Introduction

Recently, Crowdy, Mayer & Hodes (2023) introduced a concept for a thermocapillary-driven microfluidic pump that leverages asymmetries in the spacing of periodic pairs of alternating hot and cold ridges beneath a liquid suspended in the Cassie state to produce non-negligible flow rates (>1 mm/s far-field velocity) from only small differences in ridge temperatures ($<1^\circ\text{C}$). This work was motivated by Ajdari (2000), who, in a theoretical investigation, demonstrated that fluids in a locally asymmetric geometry, driven by local physical actions, exhibit a net flow. In the case of his electroosmotic pump, Ajdari showed that modulation of the surface capacitance can induce far-field pumping under a space and time periodic external electric field. In the thermocapillary pump posited by Crowdy *et al.* (2023), since surface tension is reduced on both sides of a hot ridge, liquid is driven along menisci towards the adjacent cold ones, thereby inducing flow in both directions. However, the longer meniscus, as determined by the imposed asymmetry in ridge spacing in a period window, induces a higher flow rate than the shorter one, dictating the direction of the net flow. Physically, this results in regions of recirculating (all either clockwise or anticlockwise) fluid confined close to the boundary, with a net flow far from the surface. Distinctly, when the ridges are equispaced, a pair of identical counter-rotating vortices is generated and there is zero flow in the far field. We note that vortices also form in the liquid flowing over exclusively heated superhydrophobic surfaces with ridges textured parallel (rather than transverse) to the flow (Hodes *et al.* 2017); however, the vortices generated in this configuration are orientated in a plane perpendicular to the flow direction and have been shown to negatively affect flow rates (Tomlinson *et al.* 2024). Further studies on the effects of thermocapillarity on flows over heated superhydrophobic surfaces are summarised by Crowdy *et al.* (2023).

The thermocapillary-driven pump has several advantages. First, it has no moving parts. Secondly, since the pressure field only has a modest periodic component, the Cassie state is robust. Third, there is only a periodic component of the temperature field. Previous embodiments of thermocapillary pumps required imposing a monotonic rather than periodic temperature gradient (Baier, Steffes & Hardt 2010*a,b*; Amador *et al.* 2019), which limits the length of the microchannel to a few centimetres due to freezing/boiling issues. The present thermocapillary pump does not suffer from these problems.

With these advantages in mind, one potential application for this thermocapillary pump is the direct conversion of thermal energy to mechanical work. We quantify this phenomenon by changing the semi-infinite domain considered by Crowdy *et al.* (2023) to a microchannel configuration bounded by a smooth horizontally mobile upper wall coupled to an external load. Although the following analysis is somewhat abstract, it can be readily interpreted as a simplification of a realistic configuration, i.e. the annular-geometry thermal energy-to-mechanical power converter shown in figure 1(*a*). As shown, an annulus of working liquid is trapped between a circular-perimeter superhydrophobic surface and a central, cylindrical, rotationally mobile, smooth-wall mass. The superhydrophobic surface consists of nested hot and cold ridges (fins). The hot fins are thermally coupled to an annular base (not visible in this cross-sectional view) with vertically oriented fins which penetrate gas cavities in the device. The cold fins comprise an outer surface and protrude radially inwards. One side of the working liquid is suspended in the Cassie state on the hot and cold fins and the other one contacts the smooth, inner cylindrical mass. The fin spacing is asymmetric so that a thermocapillary flow is generated, causing a shear flow to develop in the liquid, thereby imparting a torque upon the inner cylindrical mass. This torque can resist or even overcome an external torque applied to an inner axle, imparting mechanical power. (Other arrangements, such as the mass being on the outside and the superhydrophobic surface on the inside, follow.) A simplification of this geometry can be

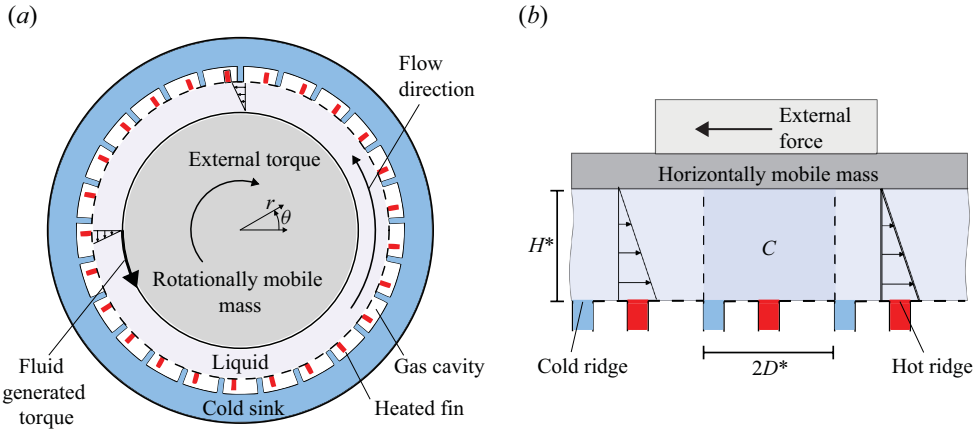


Figure 1. (a) Top view (cross-section) of a design configuration to convert thermal energy to mechanical work via thermocapillary stress along menisci. A liquid annulus resides between a smooth, solid cylinder and a superhydrophobic surface consisting of alternating hot and cold ridges (fins). (The hot fins would extend out of the page where they connect to a heat source.) Due to the counter-clockwise direction of the thermocapillary stresses along the longer menisci, the net flow is also counter-clockwise. This flow imparts a torque on the inner cylinder which can resist or overcome an external torque on it thereby imparting mechanical power; (b) an idealised two-dimensional Cartesian version of the device depicted in (a) when the inner radius of the liquid approaches the outer one, showing a periodic window denoted by C .

made by assuming the ratio of the radii of the inner and outer cylinders to be close to 1. Then, the liquid can be modelled as an infinitely periodic array of identical cells (length $2D^*$) consisting of a single pair of hot and cold ridges with accompanying menisci. The curvature is negligible so this geometry takes the form of a Cartesian microchannel of height H^* and is depicted in figure 1(b), with forces replacing torques and the motion of the wall being horizontal. A domain consisting of a single periodic cell is denoted by C .

Conveniently, a simple ordinary differential equation (ODE) couples the movement of the wall to the velocity field in the liquid. Additionally, when the mass of the wall per unit area is significantly larger than that of the liquid, the flow and temperature fields appear quasi-steady. An asymptotic solution that exhibits an exponentially small error is determined for this problem. Moreover, a simple coupling between the wall ODE and the flow problem results in exact solutions for the wall velocity and power generation. Notably, an exponentially small asymptotic error enables accurate predictions, as compared with numerical calculations, of relevant flow parameters, even when our small parameter (ratio of period of the superhydrophobic surface as per domain C in figure 1b to channel height) is as high as unity.

2. Problem description

2.1. Dimensional formulation

We consider a two-dimensional flow of a liquid of constant density ρ , viscosity μ and thermal diffusivity α in a microchannel where the top wall is smooth and horizontally mobile, has a time-dependent horizontal (parallel to the x^* coordinate) velocity $U^*(t^*)$ (and zero velocity parallel to the y^* coordinate) and is separated from the (fixed) bottom ridged (superhydrophobic) surface by a distance H^* , as per figure 2. (An asterisk indicates a dimensional variable.) The bottom surface is asymmetrically textured with alternating cold and hot ridges of length L^* at temperatures T_c^* and T_h^* , respectively, separated by (flat) menisci. Due to the periodic nature of the problem, we focus on a $2D^*$ -long period

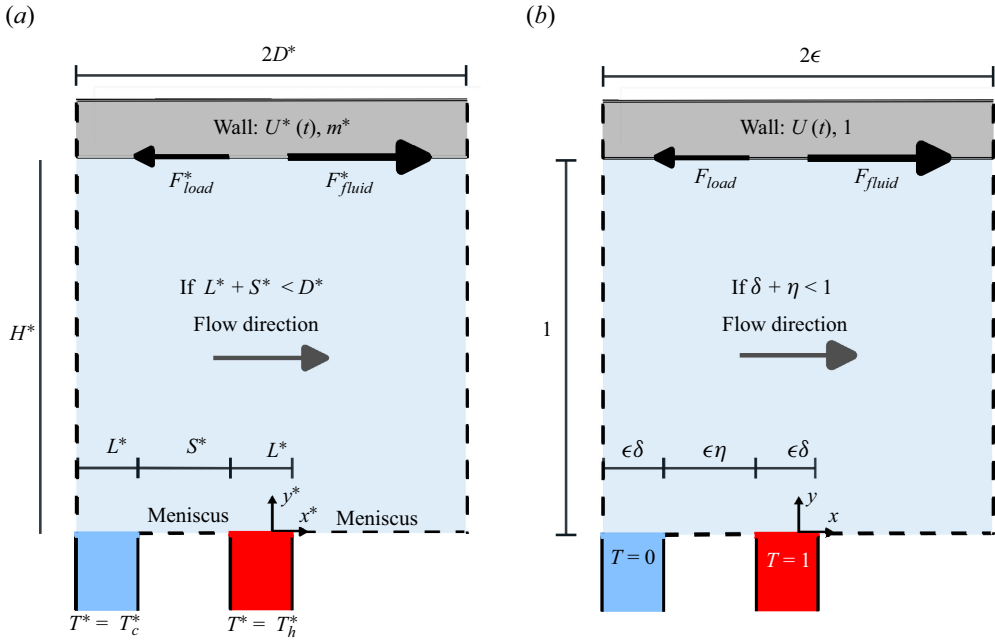


Figure 2. Schematic of a period window of the domain for (a) the dimensional problem, and (b) the dimensionless problem.

window consisting of a single pair of ridges. The cold ridge begins at $x^* = -D^*$ and the length of the meniscus between the cold and hot ridges is S^* .

In general, the fluid pressure and velocity fields are governed by mass conservation and the Navier-Stokes equations and its temperature field by the thermal energy equation (see § 2.3). We define $\mathbf{u}^* = (u^*, v^*)$ as the velocity vector with components in the x^* and y^* directions, p^* as pressure and T^* as temperature. As shown below, the flow problem is one-way coupled to the temperature problem by stress balances along menisci.

The top wall is a no-slip, adiabatic surface whose velocity is coupled to the velocity field in the liquid per Newton’s second law via the following ODE:

$$m^* \frac{dU^*}{dt^*} = -\frac{1}{2D^*} \int_{-D^*}^{D^*} \mu \left. \frac{\partial u^*}{\partial y^*} \right|_{y^*=H^*} dx^* - F_{load}^*, \quad (2.1)$$

where m^* is the mass (per unit area) of the top wall and F_{load}^* is the external load (per unit area) on the top wall. Two flat and adiabatic menisci span between the hot and cold ridges. A Marangoni stress balance along them equates the (spatial) gradient of surface tension to the viscous shear stress as per

$$\mu \left. \frac{\partial u^*}{\partial y^*} \right|_{y^*=H^*} = \beta \frac{\partial T^*}{\partial x^*}, \quad (2.2)$$

where $\beta = -d\sigma/dT^*$ is a positive constant that captures the temperature dependence of the liquid’s surface tension σ , i.e. $\sigma = \sigma_0 - \beta(T^* - T_0^*)$, where σ_0 and T_0^* are inconsequential reference values. The final conditions are that the velocity, pressure and temperature fields are periodic in the streamwise direction.

It is useful to define three engineering quantities that can be calculated from the solution to the model problem. First, the output power per unit wall area is

$$\overline{P}^* = \frac{1}{2D^*} \int_{-D^*}^{D^*} \mu \frac{\partial u^*}{\partial y^*} U^* dx, \quad (2.3)$$

i.e. the period-averaged product of the hydrodynamic friction force and wall speed. Secondly, the input power per unit wall area \overline{Q}^* is determined by integrating the heat flux through the hot ridge and dividing by the period length as per

$$\overline{Q}^* = -\frac{1}{2D^*} \int_{hot\ ridge} k \frac{\partial T^*}{\partial y^*} dx, \quad (2.4)$$

where k is the thermal conductivity of the liquid. Finally, the device efficiency is defined as

$$E = \overline{P}^* / \overline{Q}^*. \quad (2.5)$$

2.2. Discussion of forces and flow direction

With the geometry and flow-temperature problem defined, we return to discussion of the flow direction physics and forces in figure 2. First, it is useful to consider the physics when the load force F_{load}^* is absent. The hot and cold parts of the boundary at the bottom of the domain result in thermocapillary stresses that induce fluid motion. Because of the negative relationship between surface tension and increasing temperature, thermocapillary stresses cause the cold and hot ridges to attract and repel the liquid, respectively. Therefore, a rather complicated flow develops where liquid moves to the left along the meniscus of length S^* and to the right along the other meniscus (of length $2D^* - 2L^* - S^*$). These flows interact locally, generally forming 1 or 2 vortices near the bottom (superhydrophobic) surface, but, globally, a net velocity is observed approximately 1 pitch away from this surface. In turn, due to no slip and no load, the top wall moves with constant velocity. The direction of this velocity is determined by the longer meniscus so that if $2D^* - 2L^* - S^* > S^*$ or $L^* + S^* < D^*$, as seen in figure 2(a), flow moves left-to-right and when $2D^* - 2L^* - S^* < S^*$ flow moves right-to-left.

Inclusion of the load further complicates the physics. Of course, arbitrary assignment of F_{load}^* yields a valid physical solution, but in the context of energy conversion we are particularly interested in situations where the external load is driven only by the flow generated by thermocapillary stresses. For this to be true (for a given geometry and temperature difference) two requirements of F_{load}^* are needed. The first is that the drag generated by the thermocapillary stresses and the external load must have opposite signs to work against each other. The second is that F_{load}^* must be less than or equal to in magnitude the largest possible drag force generated by the thermocapillary stresses, a quantity that can be determined exactly from solutions discussed later. This is because, if the applied external load exceeds this maximum force, the wall will move in the direction of the applied external load. In this case, the wall can be viewed as driving the liquid flow instead of the flow driving the wall. Then thermocapillary stresses may help to resist wall motion; however, the system can no longer be considered capable of providing power to external devices.

2.3. Non-dimensional formulation

It is natural to non-dimensionalise lengths with H^* , velocities with a characteristic velocity scaling $U_c^* = \Delta T^* \beta / \mu$, where $\Delta T^* = T_h^* - T_c^*$, according to the shear stress balances

along the menisci, and pressure with $\mu U_c^*/H^*$. Since this problem is in a microfluidic configuration, the limiting temporal behaviour (i.e. the slowest time scale) is expected to be that of the upper wall. Therefore, time is rescaled with m^*H^*/μ , as follows from (2.1). The governing equations in the fluid (conservation of mass, momentum and thermal energy) become

$$\nabla \cdot \mathbf{u} = 0, \tag{2.6}$$

$$M \frac{\partial \mathbf{u}}{\partial t} + Re (\mathbf{u} \cdot \nabla \mathbf{u}) = -\nabla p + \nabla^2 \mathbf{u}, \tag{2.7}$$

$$MPr \frac{\partial T}{\partial t} + PrRe (\mathbf{u} \cdot \nabla T) = \nabla^2 T, \tag{2.8}$$

where $Re = \rho \Delta T^* \beta H^*/\mu^2$ is the Reynolds number, $Pr = \mu/(\alpha\rho)$ is the Prandtl number and $M = (\rho H^*)/m^*$ is a parameter that compares the mass of the liquid with that of the wall (per unit area in the x and z (out of plane) directions). The boundary conditions on the top wall are

$$\mathbf{u} = U(t), \quad \frac{\partial T}{\partial y} = 0 \quad \text{at } y = 1. \tag{2.9}$$

In the ODE governing the wall velocity (2.1) the load force (per unit area) is non-dimensionalised using $\mu U_c^*/H^*$, yielding

$$\frac{dU}{dt} = -\frac{1}{2\epsilon} \int_{-\epsilon}^{\epsilon} \frac{\partial u}{\partial y} \Big|_{y=1} dx - F_{load}, \tag{2.10}$$

where $\epsilon = D^*/H^*$ is the aspect ratio of the domain. On the bottom superhydrophobic surface the boundary conditions are

$$\mathbf{u} = 0, \quad T = 0 \quad \text{for } y = 0, \quad -\epsilon < x < -\epsilon(1 - \delta), \tag{2.11}$$

$$\mathbf{u} = 0, \quad T = 1 \quad \text{for } y = 0, \quad -\epsilon(1 - \delta - \eta) < x < -\epsilon(1 - 2\delta - \eta), \tag{2.12}$$

$$\frac{\partial u}{\partial y} = \frac{\partial T}{\partial x}, \quad \frac{\partial T}{\partial y} = 0 \quad \text{for } y = 0, \quad -\epsilon(1 - \delta) < x < -\epsilon(1 - \delta - \eta), \tag{2.13}$$

$$\frac{\partial u}{\partial y} = \frac{\partial T}{\partial x}, \quad \frac{\partial T}{\partial y} = 0 \quad \text{for } y = 0, \quad -\epsilon(1 - 2\delta - \eta) < x < \epsilon, \tag{2.14}$$

where $\delta = L^*/D^*$ is the solid fraction of the hot or cold ridges and $\eta = S^*/D^*$ is the fraction of a half-period attributable to the leftmost meniscus. In addition, periodicity is enforced for the velocity, pressure and temperature fields at $x = \pm\epsilon$.

Finally, \bar{P}^* is rescaled using $\mu U_c^{*2}/H^*$ and Q^* using $k\Delta T^*/H^*$ so that

$$\bar{P} = \frac{1}{2\epsilon} \int_{-\epsilon}^{\epsilon} \frac{\partial u}{\partial y} U dx, \tag{2.15}$$

and

$$\bar{Q} = -\frac{1}{2\epsilon} \int_{hot\ ridge} \frac{\partial T}{\partial y} dx. \tag{2.16}$$

The efficiency can be written in terms of the dimensionless quantities as

$$E = \Omega \frac{\bar{P}}{\bar{Q}}, \tag{2.17}$$

where $\Omega = \beta^2 \Delta T^*/(\mu k)$.

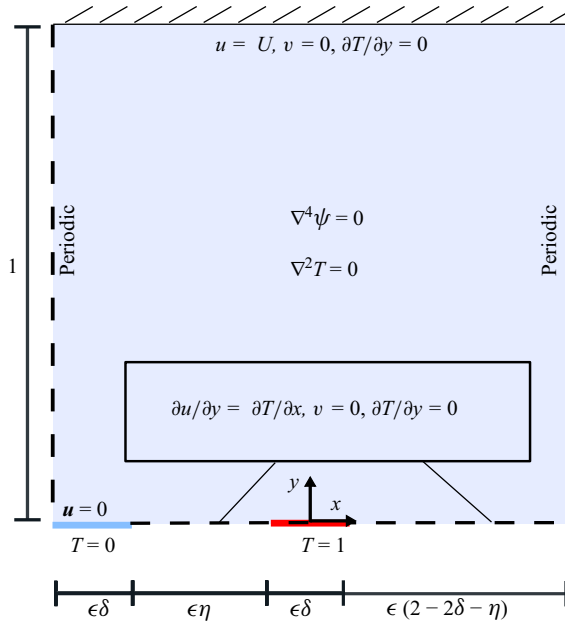


Figure 3. Problem to solve after low Reynolds number and large mass assumptions. The fluid and temperature fields are quasi-steady; therefore, the solution needed is simplified to that of a flow with a prescribed wall velocity at the top of the domain.

3. Theoretical analysis

Our purpose is to gain theoretical insight into the transfer of thermal energy into mechanical power. To proceed, the Reynolds number is assumed to be vanishingly small, as is common in microfluidic devices. Furthermore, the assumption that $M \ll 1$ is invoked, meaning that the mass of the liquid is small compared with that of the wall. Taking the limits $M, Re \rightarrow 0$ in (2.6)–(2.8) leads to the equations

$$\frac{\partial^2 T}{\partial x^2} + \frac{\partial^2 T}{\partial y^2} = 0 \quad \text{and} \quad \frac{\partial^4 \psi}{\partial x^4} + \frac{\partial^4 \psi}{\partial x^2 \partial y^2} + \frac{\partial^4 \psi}{\partial y^4} = 0, \tag{3.1}$$

where $\psi = \psi^*/(U_c^* H^*)$ is a streamfunction defined such that

$$u = \frac{\partial \psi}{\partial y}, \quad v = -\frac{\partial \psi}{\partial x}. \tag{3.2}$$

This stream function is coupled to the wall velocity governed by (2.10) via the no-slip condition. The large mass assumption enables a significant simplification of our analysis, as the thermal energy and flow equations appear quasi-static. Furthermore, the assumption of small Re (and thus also small Péclet number $Pe = RePr$) removes the two-way coupling of the velocity and temperature fields, instead allowing the (now steady) Laplacian thermal problem to be resolved first, followed by the (quasi-steady) Stokes problem. The quasi-steady nature of the flow problem means that we need only resolve the flow for a given upper wall velocity U , as depicted in figure 3. This can be done in closed form, and the consequent shear stress on the upper wall simply inserted into the ODE governing the wall's motion.

3.1. Small period limit

A further assumption is needed to facilitate the analysis: that the period length is much smaller than the channel height, an oft-valid assumption for microchannels textured with superhydrophobic surfaces. This limit, corresponding to $\epsilon \rightarrow 0$, is the same one recently considered by Hodes *et al.* (2023) for the conventional transverse ridge problem, in the absence of thermocapillary stress, when the ridges are no-slip, diabatic (isoflux) and equally spaced, and the microchannel is symmetrically textured. To make the location of boundary conditions (2.11)–(2.14) independent of ϵ , we rescale x according to $X = x/\epsilon$. The governing equations transform to

$$\frac{1}{\epsilon^2} \frac{\partial^2 T}{\partial X^2} + \frac{\partial^2 T}{\partial y^2} = 0 \quad \text{and} \quad \frac{1}{\epsilon^4} \frac{\partial^4 \psi}{\partial X^4} + \frac{2}{\epsilon^2} \frac{\partial^4 \psi}{\partial X^2 \partial y^2} + \frac{\partial^4 \psi}{\partial y^4} = 0. \quad (3.3)$$

3.1.1. Outer problem

In the limit as $\epsilon \rightarrow 0$, the outer region corresponds to fixing our location in the channel and keeping $X, y = O(1)$. It is typical at this point to expand the streamfunction in the small parameter ϵ and determine a unique solution at each order of this parameter. However, solutions of the Laplace and biharmonic equations that exhibit small-scale periodicity (that is, not simply uniform) in X will exhibit exponential variation in y . To match with an inner solution near $y = 0$ would necessitate this variation be exponentially small. As we are not concerned with these exponentially small orders, we only consider the solutions constant in X , and posit the streamfunction expansion

$$\psi = \psi_{out}(y, \epsilon) + \text{e.s.t.}, \quad (3.4)$$

where e.s.t. refers to exponentially small terms. Substituting (3.4) into (3.3) this satisfies

$$\frac{d^4 \psi_{out}}{dy^4} = 0. \quad (3.5)$$

Furthermore, if we integrate the x -momentum equation and apply periodicity of pressure (i.e. there is no linear component), then $d^3 \psi_{out}/dy^3 = 0$. Thus integrating this, applying the no-slip condition at the top ($d\psi_{out}/dy = U$ at $y = 1$), and choosing $\psi_{out} = 0$ at $y = 0$, we find that

$$\psi_{out} = \frac{C(\epsilon)}{2}(2y - y^2) + Uy, \quad (3.6)$$

where $C(\epsilon)$ is an ϵ -dependent constant. A similar assumption for the temperature, $T = T_{out}(y, \epsilon) + \text{e.s.t.}$, leads to an outer solution independent of y , that is, $T = D(\epsilon) + \text{e.s.t.}$, where $D(\epsilon)$ is, again an ϵ -dependent constant.

3.1.2. Inner problem

Near the bottom superhydrophobic surface, the flow and thermal problems are two-dimensional and require a different solution. Here, $x, y \sim \epsilon$ and all the terms in the Stokes equation balance. It is therefore natural to use inner variables $X = x/\epsilon$ and $Y = y/\epsilon = O(1)$. Writing $\psi = \Psi(X, Y, \epsilon) + \text{e.s.t}$ and $T = \Theta(X, Y, \epsilon) + \text{e.s.t.}$, the inner problem for the temperature Θ is given by

$$\frac{\partial^2 \Theta}{\partial X^2} + \frac{\partial^2 \Theta}{\partial Y^2} = 0, \quad Y > 0, \quad -1 < X < 1, \quad (3.7)$$

$$\frac{\partial \Theta}{\partial Y} = 0, \quad Y = 0, \quad \text{on menisci}, \quad (3.8)$$

$$\Theta = 1, \quad Y = 0, \quad \text{on hot ridge}, \quad (3.9)$$

$$\Theta = 0, \quad Y = 0, \quad \text{on cold ridge}, \quad (3.10)$$

with periodicity at $X = \pm 1$, and the matching condition with the constant solution in the outer region, or, alternatively, the adiabatic matching condition

$$\frac{\partial \Theta}{\partial Y} \rightarrow 0, \quad Y \rightarrow \infty. \quad (3.11)$$

Given Θ , then the inner problem for Ψ becomes

$$\frac{\partial^4 \Psi}{\partial X^4} + 2 \frac{\partial^4 \Psi}{\partial X^2 \partial Y^2} + \frac{\partial^4 \Psi}{\partial Y^4} = 0, \quad Y > 0, \quad -1 < X < 1, \quad (3.12)$$

$$\frac{\partial^2 \Psi}{\partial Y^2} = \epsilon \frac{\partial \Theta}{\partial X}, \quad Y = 0, \quad \text{on interfaces} \quad (3.13)$$

$$\frac{\partial \Psi}{\partial Y} = 0, \quad Y = 0, \quad \text{on ridges} \quad (3.14)$$

$$\Psi = 0, \quad Y = 0, \quad -1 < X < 1 \quad (3.15)$$

with periodic conditions at $X = \pm 1$. The final condition on Ψ comes from matching, as $Y \rightarrow \infty$, with the outer solution as $y \rightarrow 0$ as per

$$\frac{\partial \Psi}{\partial Y} \sim \epsilon U + \epsilon(1 - \epsilon Y)C(\epsilon), \quad Y \rightarrow \infty. \quad (3.16)$$

This problem has two inhomogeneous boundary conditions, the forcing due to temperature gradients along the interface and the matching condition as $Y \rightarrow \infty$. Since it is linear in Ψ , the solution can be decomposed into two parts

$$\Psi = \epsilon (\Psi_1 + \Psi_2), \quad (3.17)$$

where Ψ_1 satisfies

$$\frac{\partial^4 \Psi_1}{\partial X^4} + 2 \frac{\partial^4 \Psi_1}{\partial X^2 \partial Y^2} + \frac{\partial^4 \Psi_1}{\partial Y^4} = 0, \quad Y > 0, \quad -1 < X < 1, \quad (3.18)$$

$$\frac{\partial^2 \Psi_1}{\partial Y^2} = \frac{\partial \Theta}{\partial X}, \quad Y = 0, \quad \text{on interfaces}, \quad (3.19)$$

$$\frac{\partial \Psi_1}{\partial Y} = 0, \quad Y = 0, \quad \text{on ridges}, \quad (3.20)$$

$$\Psi_1 = 0, \quad Y = 0, \quad -1 < X < 1, \quad (3.21)$$

$$\frac{\partial \Psi_1}{\partial Y} \sim U_{pump}, \quad Y \rightarrow \infty, \quad (3.22)$$

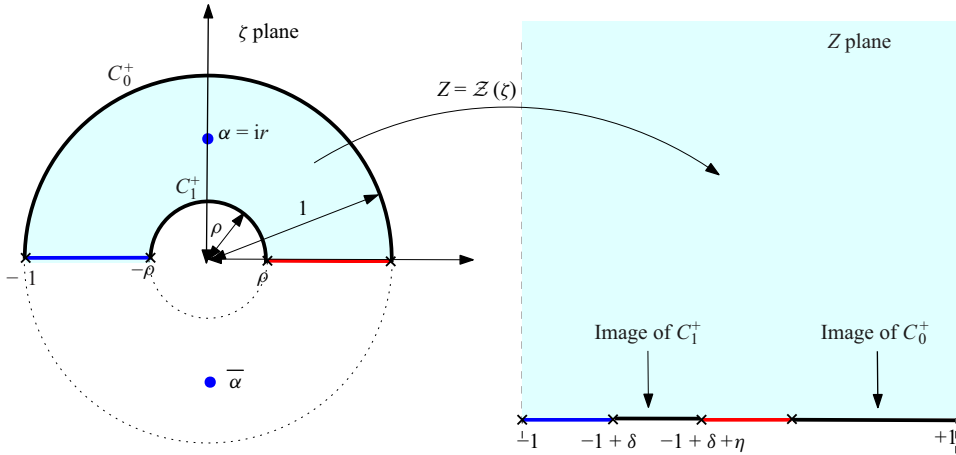


Figure 4. Conformal mapping from an upper half-annulus $\rho < |\zeta| < 1, \text{Im}[\zeta] > 0$ in a parametric ζ plane to a single period window of the inner problem.

where U_{pump} is a constant to be found, and Ψ_2 satisfies

$$\frac{\partial^4 \Psi_2}{\partial X^4} + 2 \frac{\partial^4 \Psi_2}{\partial X^2 \partial Y^2} + \frac{\partial^4 \Psi_2}{\partial Y^4} = 0, \quad -1 < X < 1, 0 < Y \tag{3.23}$$

$$\frac{\partial^2 \Psi_2}{\partial Y^2} = 0, \quad \text{on interfaces, } Y = 0 \tag{3.24}$$

$$\frac{\partial \Psi_2}{\partial Y} = 0, \quad \text{on ridges, } Y = 0 \tag{3.25}$$

$$\Psi_2 = 0, \quad -1 < X < 1, Y = 0 \tag{3.26}$$

$$\frac{\partial \Psi_2}{\partial Y} \sim (U - U_{pump}) + (1 - \epsilon Y)C(\epsilon), \quad Y \rightarrow \infty, \tag{3.27}$$

both with periodic conditions at $X = \pm 1$. We remark that U_{pump} can be interpreted physically as the far-field pump velocity when the upper wall is infinitely far away (see Crowdy *et al.* 2023).

The problem for Ψ_1 turns out to be exactly that already considered by Crowdy *et al.* (2023), meaning that the results there can be imported for reuse here. Defining a complex variable $Z = X + iY$, then Θ and Ψ_1 can be written in terms of a parametric conformal mapping variable ζ taking values in an upper half-annulus $\rho < |\zeta| < 1, \text{Im}[\zeta] > 0$. A correspondence between ζ and the physical variable Z , as depicted in figure 4 using colour coding to reflect correspondences, is furnished by the following conformal mapping function:

$$Z = \mathcal{Z}(\zeta) = -\frac{i}{\pi} \log \left[R \frac{P(\zeta/\alpha, \rho)P(\alpha\zeta, \rho)}{P(\zeta/\bar{\alpha}, \rho)P(\bar{\alpha}\zeta, \rho)} \right], \tag{3.28}$$

where

$$R = \exp(-i\pi) \frac{P(-1/\bar{\alpha}, \rho)P(-\bar{\alpha}, \rho)}{P(-1/\alpha, \rho)P(-\alpha, \rho)}. \tag{3.29}$$

This differs from that of Crowdy *et al.* (2023) only in the choice of the constant R , which is chosen here to impose that $\mathcal{Z}(-1) = -1$. The special function $P(\zeta, \rho)$ is defined by the infinite product

$$P(\zeta, \rho) \equiv (1 - \zeta) \prod_{n=1}^{\infty} (1 - \rho^{2n} \zeta)(1 - \rho^{2n} / \zeta), \quad (3.30)$$

which is convergent for $0 \leq \rho < 1$; this function is closely related to the so-called prime function of the annulus $\rho < |\zeta| < 1$ (Crowdy 2020). The point $\alpha = ir$ lies on the imaginary axis, this being necessary to ensure that the two ridges are of the same length. The upper half-unit circle, denoted by C_0^+ , and the upper half-circle $|\zeta| = \rho$, denoted by C_1^+ , are mapped to the two menisci. The above formulae depend on two real parameters, ρ and r , which are determined by the geometry of the ridge–menisci arrangement in each period window. Indeed, two nonlinear algebraic expressions enable the calculation of ρ and r for specified values of δ and η as per

$$\mathcal{Z}(-\rho) = -1 + \delta, \quad \mathcal{Z}(\rho) = -1 + \delta + \eta. \quad (3.31)$$

These are easily solved using Newton’s method.

With this correspondence in place, Crowdy *et al.* (2023) determined that the temperature field is given in terms of the parametric variable ζ by

$$\Theta = 1 - \frac{\arg[\zeta]}{\pi}, \quad (3.32)$$

and the associated streamfunction by

$$\Psi_1 = \text{Im}[(\bar{Z} - Z)f_1(\zeta)], \quad (3.33)$$

where

$$f_1(\zeta) = \frac{i}{4} \left[\frac{1}{2} + \sum_{n=1}^{\infty} \frac{2}{1 + \rho^n} \left(\frac{1 - (-1)^n}{(\pi n)^2} \right) \left(\zeta^n + \frac{\rho^n}{\zeta^n} \right) \right]. \quad (3.34)$$

Moreover, from a far-field analysis as $Y \rightarrow \infty$ of $\partial\Psi_1/\partial Y$, the pumping speed is found to be

$$U_{pump} = \frac{2}{\pi^2} \left[\sum_{m=1}^{\infty} \frac{(-1)^{m+1}}{(2m - 1)^2(1 + \rho^{2m-1})} \left(r^{2m-1} - \left(\frac{\rho}{r}\right)^{2m-1} \right) \right]. \quad (3.35)$$

Conveniently, the solution for Ψ_2 can also be found in terms of the same parametric variable ζ . The boundary value problem determining Ψ_2 is similar to that of a linear shear flow over a superhydrophobic surface as resolved in a separate study by Crowdy (2011), who generalised solutions due to Philip (1972*a*) for transverse shear flow over a periodic superhydrophobic surfaces with a single meniscus per period. The analysis of Crowdy (2011) allows for any finite number of menisci per period of the surface, including the case of two unequal menisci which is precisely the geometry relevant in the present problem. To cast it into a form whereby the results of Crowdy (2011) can be imported for use here, we define $\Psi_2 = -\epsilon C(\epsilon)\tilde{\Psi}_2$ so that

$$\frac{\partial\tilde{\Psi}_2}{\partial Y} \sim Y - \frac{1}{\epsilon} \left(1 + \frac{U - U_{pump}}{C(\epsilon)} \right). \quad (3.36)$$

From Crowdy (2011), the solution for $\tilde{\Psi}_2$ can be found with the same machinery as used for Ψ_1 and, in particular, the solution can also be written as a function of the same parametric variable ζ . It is

$$\tilde{\Psi}_2 = \text{Im}[(\bar{Z} - Z)g(\zeta)], \quad \text{where } g(\zeta) = \frac{1}{4\pi} \log \left[\frac{P(\zeta/\alpha, \rho)P(\zeta\bar{\alpha}, \rho)}{P(\zeta/\bar{\alpha}, \rho)P(\zeta\alpha, \rho)} \right], \quad (3.37)$$

and, as $Y \rightarrow \infty$

$$\frac{\partial \tilde{\Psi}_2}{\partial Y} \sim Y + \lambda_{\perp} \quad \text{where} \quad \lambda_{\perp} = \frac{1}{\pi} \log \left| \frac{P(\alpha^2, \rho)}{P(|\alpha|^2, \rho)} \right|, \quad (3.38)$$

has an interpretation as the hydrodynamic slip length of the superhydrophobic surface (Crowdy 2011). Equating the two far-field conditions, (3.36) and (3.38), necessitates that

$$\lambda_{\perp} = -\frac{1}{\epsilon} \left(1 + \frac{U - U_{pump}}{C(\epsilon)} \right). \quad (3.39)$$

Therefore $C(\epsilon) = (U_{pump} - U)/(1 + \epsilon\lambda_{\perp})$ and

$$\Psi \sim \epsilon\Psi_1 + (U - U_{pump}) \frac{\epsilon^2}{1 + \epsilon\lambda_{\perp}} \tilde{\Psi}_2. \quad (3.40)$$

3.1.3. Shear stress and a composite solution

With $C(\epsilon)$ known, the outer solution (3.4) becomes

$$\psi_{out} = \frac{U_{pump} - U}{1 + \epsilon\lambda_{\perp}} \left(y - \frac{1}{2}y^2 \right), \quad (3.41)$$

which directly yields the shear stress at the top wall ($y = 1$) as

$$\frac{\partial u}{\partial y} = \frac{\partial^2 \psi_{out}}{\partial y^2} = \frac{U - U_{pump}}{1 + \epsilon\lambda_{\perp}}. \quad (3.42)$$

A composite solution is constructed by adding the outer and inner solutions and subtracting that in the overlap region. Fortunately, the outer solution is a power series in ϵ and Y (λ_{\perp} is at most $O(1)$), so it retains its form through the overlap region if all orders are included, meaning it is precisely the overlap solution. Thus, the composite solution is simply the inner solution, written in terms of outer variables,

$$\psi_{comp} = \Psi(x/\epsilon, y/\epsilon, \epsilon). \quad (3.43)$$

3.2. Wall dynamics and power

Inserting the outer asymptotic solution for $\partial u/\partial y = \partial^2 \psi/\partial y^2$ into the ODE governing the wall motion (2.10) yields

$$\frac{dU}{dt} = \frac{U_{pump} - U}{1 + \epsilon\lambda_{\perp}} - F_{load}. \quad (3.44)$$

Until now, F_{load} has been deliberately left ambiguous to highlight the generality of this ODE. However, we now focus on the case when F_{load} is a constant.

When the initial condition is $U(0) = U_{pump}$ (the steady solution without load), then the solution applying constant load F_{load} for $t > 0$ is

$$U = U_{pump} - F_{load} (1 + \epsilon\lambda_{\perp}) \left[1 - \exp \left(-\frac{t}{1 + \epsilon\lambda_{\perp}} \right) \right]. \quad (3.45)$$

This results corresponds to the application of a load when the top wall is already moving at velocity U_{pump} and leads to some relevant physical parameters. First, we define a maximum load that can be supported by the thermocapillary pump by constraining F_{load} . In particular, we impose that F_{load} is in the opposite direction of the thermocapillary-induced pumping velocity U_{pump} (thus acting as a resistance) and $|F_{load}| \leq |U_{pump}|/$

$(1 + \epsilon\lambda_{\perp})$ so that $U > 0$ in all cases. If there is equality, then $|F_{load}| = |U_{pump}|/(1 + \epsilon\lambda_{\perp})$, and (3.45) tends to the steady-state $U = 0$ as $t \rightarrow \infty$. Hence, we refer to this as the maximum load that can be supported – if it is any larger, the wall will move against the pumping flow at steady state. Alternatively, $|U_{pump}|/(1 + \epsilon\lambda_{\perp})$ can be interpreted as the fluid force on an immobile (or pinned) wall.

We now consider power generation. Denoting the average shear stress from the fluid on the wall as F_{fluid} and multiplying (3.44) by U , conservation of energy for the wall takes the form

$$\frac{d}{dt} \left(\frac{1}{2} U^2 \right) = F_{fluid} U - F_{load} U = \bar{P} - \bar{P}_{load}. \quad (3.46)$$

The term \bar{P} is the (average) power from the thermocapillary flow delivered to the wall (defined earlier in (2.15)), and \bar{P}_{load} is the mechanical power output from the wall to the load. (Note that no averaging of the asymptotic solution is actually needed, since the outer solution is uniform in x .) During the transient, \bar{P} and \bar{P}_{load} will not be equal in general, as some energy is going to/coming from the changes in kinetic energy of the wall. But at steady state the powers must balance; therefore, $\bar{P} = \bar{P}_{load} = F_{load} U$. Thus, \bar{P} is the “steady output power”.

Inserting the asymptotic approximation for shear stress into the definition (2.15) of (instantaneous) fluid power gives

$$\bar{P} \sim \frac{U(U_{pump} - U)}{1 + \epsilon\lambda_{\perp}}, \quad \epsilon \ll 1. \quad (3.47)$$

Notably, this implies that the maximum fluid power will always occur when $U = U_{pump}/2$, taking the value

$$\bar{P}_{max} \sim \frac{U_{pump}^2}{4(1 + \epsilon\lambda_{\perp})}, \quad \epsilon \ll 1. \quad (3.48)$$

If at steady state (set (3.44) to zero and substitute $U = U_{pump}/2$), this requires that $F_{load} = U_{pump}/[2(1 + \epsilon\lambda_{\perp})]$. Alternatively, since $\bar{P} = \bar{P}_{load}$ at steady state, one can substitute this F_{load} expression into $F_{load} U$ and derive the same maximum power.

From an expression for the heat rate through the hot ridge from Crowdy *et al.* (2023) the thermal power input to the fluid from the hot ridge is given by

$$\bar{Q} = \frac{1}{2\pi\epsilon} \log \rho, \quad (3.49)$$

where ρ is a geometric parameter related to δ and η (but not ϵ). It is notable that \bar{P} is only weakly dependent on ϵ , but \bar{Q} scales with $1/\epsilon$. The second observation can be easily explained because, for a fixed channel height, making ϵ smaller is akin to making the period smaller. This brings the cold and hot ridges closer together; therefore, more heat is required to maintain the imposed temperature difference between the hot and cold ridges. Power only weakly depending on ϵ stems from the fact that thermocapillary pumping also depends weakly on ϵ . This is not the case for calculated slip lengths for shear flows over a mixed no-slip/no-shear surface, where the far-field velocity increment scales linearly with ϵ (Philip 1972*b*). The difference here is the inclusion of thermocapillary stress which itself scales like $1/\epsilon$, growing as ϵ gets smaller and the ridges approach each other. This, combined with the fact that the menisci lengths scale with ϵ , yields an $O(1)$ quantity and

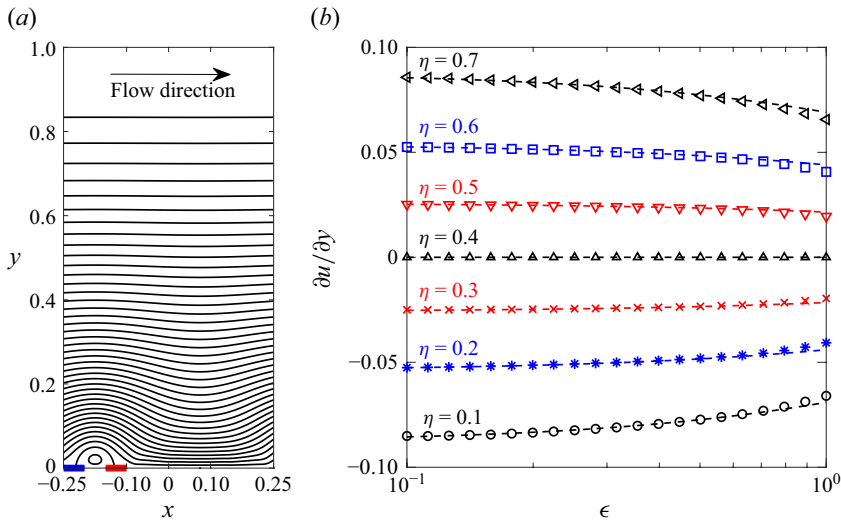


Figure 5. (a) Asymptotic streamlines for a flow with a stationary upper wall, $\epsilon = 0.25$, $\eta = 0.1$ and $\delta = 0.1$. (b) Dimensionless (upper) wall shear stress (3.42) versus (half) period width (ϵ) when upper wall is stationary ($U = 0$) and the solid fraction (δ) is 0.1. Dashed curves are the full asymptotic results and symbols the numerical results.

a power output with only a weak dependence on ϵ . Finally, an expression for efficiency can be derived as

$$E \sim 2\pi\epsilon\Omega \frac{U(U_{pump} - U)}{(1 + \epsilon\lambda_{\perp}) \log \rho}. \quad (3.50)$$

4. Results

4.1. Fixed wall

First, we look at the flow when the upper wall is stationary. Figure 5(a) plots streamlines from (3.43) when $\epsilon = 0.25$, $\eta = 0.1$ and $\delta = 0.1$. This set-up generates a flow from left-to-right which rolls over a vortex centred above the shorter meniscus. The flow is fastest near the superhydrophobic surface at the bottom and then tapers out to a linear shear flow that approaches zero velocity as $y \rightarrow 1$. The shear stress at the top wall can be estimated using the outer solution (3.42) and this is plotted in figure 5(b) as a function of ϵ for $\delta = 0.1$ and discrete values of η . The asymptotic results for $\partial u / \partial y$ at $y = 1$ are represented by the dashed curves and the symbols are (exact) numerical results. For the numerical analysis we used a pseudospectral method (Trefethen 2000) which closely followed work by Game, Hodes & Papageorgiou (2019) and Mayer, Kadoko & Hodes (2021) that is outlined in the supplemental information. The numerical method solves Laplace’s equation for the temperature field and the biharmonic equation for the velocity, relaxing the assumption that $\epsilon \ll 1$. There is remarkable agreement up to at least $\epsilon = 0.5$ where the domain is square. Notably, as ϵ increases the shear stress decreases due to the increasing impact of the inner problem. This is because this limit corresponds to the period length growing for fixed channel height. In such a scenario, the fluid does not have the space to fully develop into a one-dimensional flow and some of the wall stress acts normal to the upper wall. In Stokes flow with no pressure gradient a global force balance requires the total shear stress around the boundary integrates to zero. This means the normal stress results in a loss of beneficial tangential shear stress. Essentially some of the stress is being used to push into

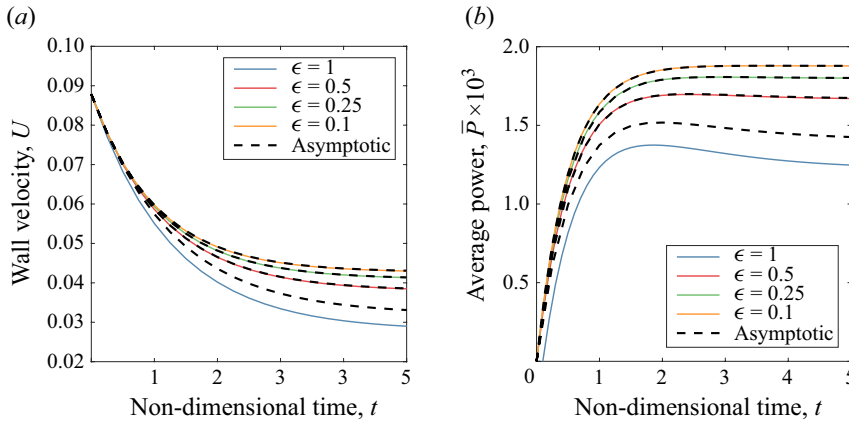


Figure 6. (a) Dimensionless wall velocity versus time for $\delta = 0.1$ and $\eta = 0.1$. (b) Instantaneous dimensionless fluid power per unit wall area over time for $\delta = 0.1$ and $\eta = 0.1$. Solid lines are numerical solutions for arbitrary ϵ . The numerical method solves (2.10) with the fluid shear stress determined by solutions of the biharmonic equation.

the wall vertically rather than drag it horizontally, leading to a loss in efficiency. Finally, the magnitude of the shear stress increases with $|0.5 - \delta - \eta|$ because the deleterious impact of the shorter meniscus is minimised.

4.2. Transient behaviour

Next, the wall is allowed to move according to the ODE defined in (2.10). Figure 6(a) shows the wall velocity versus time for $\epsilon = 0.1, 0.25, 0.5$ and 1 and figure 6(b) the corresponding average dimensionless power per wall area. In all cases $F_{load} = U_{pump}/2$, the force (per unit area) yields the highest steady-state power output when $\epsilon = 0$. Since this value also gives the maximal steady power for any choice of ϵ , it serves as a good datum for performance. Additionally, by keeping the dimensionless force constant, the effect of ϵ on the power (per unit area) can be more easily visualised. In figure 6 the solid lines are numerical solutions, and the black dashed lines are the asymptotic solutions given by (3.45) and (3.47). The numerical method still maintains that $M \ll 1$ and therefore solves (2.10); however, the shear stress is calculated by solving the biharmonic equation for a given wall velocity, which is outlined in detail in the supplemental information. They show remarkable agreement for $\epsilon \leq 0.5$ and even adequate agreement for $\epsilon = 1$. In figure 6(a) it is clear that increasing ϵ leads to a more rapid deceleration and smaller steady-state velocity for the wall, consistent with the decrease in dimensionless shear stress as ϵ grows observed in figure 5. In figure 6(b) the effect of ϵ is again to decrease the dimensionless output, with larger values displaying less dimensionless power. For $\epsilon = 1$, the wall velocity is slowed enough to drop significantly below $U_{pump}/2$ and therefore cause the power to cross its peak value and tend to a lower value as $t \rightarrow \infty$.

4.3. Steady-state power: effect of δ and η

Now the effects of δ and η are examined: recall that δ is the width of the ridges and η is the width the menisci to the right of the cold ridge (see figure 2), normalised by half a period. As mentioned earlier and inferred from (3.47), for a given geometric set-up the maximum power will always occur when $U = U_{pump}/2$, which can be ensured at steady state if $F_{load} = U_{pump}/[2(1 + \epsilon\lambda_{\perp})]$. We focus on this case to examine the effects of δ and η in figure 7, which displays contour plots of the asymptotic solutions for three

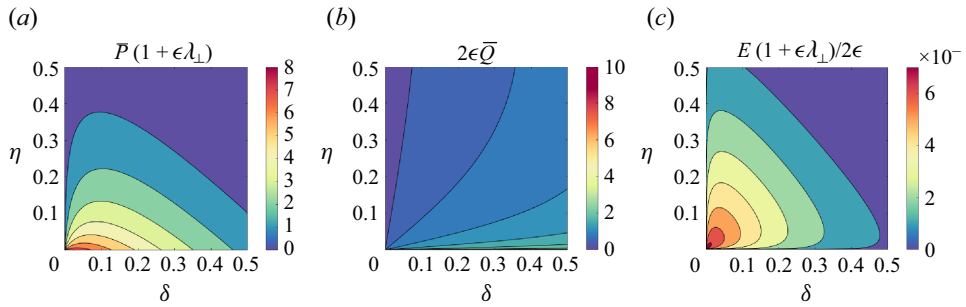


Figure 7. (a) Contour of asymptotic solutions to leading-order steady power output as a function of δ and η when $F_{load} = U_{pump}/[2(1 + \epsilon\lambda_{\perp})]$. This value of external load is chosen to maximise the power output; (b) corresponding contour plot of the asymptotic solution to total heat rate. This is singular as $\eta \rightarrow 0$, reflected by the sharp gradient in shading.; (c) corresponding contour plot of the asymptotic solution to normalised efficiency.

relevant quantities. Figure 7(a) shows $\bar{P}(1 + \epsilon\lambda_{\perp})$, which is the power output per unit wall area normalised such that it only depends on δ and η . It is exactly the leading-order power output for small ϵ . One observation is that, for a fixed δ , higher power is achieved for smaller values of η , increasing monotonically. This is because, in this limit, the small meniscus (deleterious to the flow) is shrinking and the longer meniscus (driving the flow) is growing, leading to enhanced thermocapillary pumping.

For a fixed η , however, the behaviour as δ gets smaller is more interesting: the power output increases as δ decreases when $\delta \gtrsim \eta$, but then decreases when $\delta \lesssim \eta$. This has to do in part with the relative changes to the length of the longer meniscus, which is $2 - 2\delta - \eta$. When $\delta \gg \eta$, then $2 - 2\delta - \eta \approx 2 - 2\delta$, which is sensitive to changes in δ . Therefore, as δ gets smaller and $\delta \gg \eta$, power grows because the longer meniscus is lengthened, increasing thermocapillary pumping. However, when $\eta \gg \delta$, then the length of the long meniscus becomes $2 - 2\delta - \eta \approx 2 - \eta$, which is insensitive now to changes in δ , and the length approaches an upper bound. As the benefit of lengthening the long meniscus is lost, a secondary disadvantageous effect becomes important concerning interfacial temperature gradients.

As δ gets smaller the local heat fluxes near the triple contact points get larger. Since the average temperature gradient is fixed by the (prescribed) temperature drop, this means that the magnitude of temperature gradients at the centre of the menisci decrease. Crucially, stresses at the centre of menisci are the most important for generating flows, leading to decreases in the flow contributions from both the longer and shorter menisci. However, because the smaller menisci are less impactful than the larger, the net effect is that overall pumping rates are decreased. This degradation can be fairly significant when $\delta < \eta$. As a consequence, for maximum power the advice would be to choose $\eta \ll \delta \ll 1$.

Figure 7(b) depicts the dimensionless heat load through the hot ridge, per unit depth. It is singular as $\eta \rightarrow 0$ because two isothermal regions of different temperatures are forced to approach each other. Conversely, as $\delta \rightarrow 0$, the heat load tends towards zero as the overall area for heat to enter the domain vanishes.

Finally, figure 7(c) depicts the efficiency (2.17) normalised such that it only depends on η and δ , not ϵ . Interestingly, the high power values near $\eta = 0$ in figure 7(a) are neutralised by the larger heat load required to maintain this state in figure 7(b). Also, the lower heat requirements near $\delta = 0$ in figure 7(b) correspond to weaker regions of power generation in figure 7(a). Consequently, to achieve the best efficiency the advice would be to set $\delta \approx \eta$ and make them as small as possible. This is conveniently also bordering the high power regime in figure 7(a) and therefore advantageous for two reasons.

5. Concluding remarks

One consequence of the above discussion is the importance of the parameter $\Omega = \beta^2 \Delta T^* / (k\mu)$ on the efficiency of the device, E . Recall, Ω is a parameter that first appears in (2.17) as a coefficient of proportionality for the efficiency. Therefore, to maximise efficiency it is of benefit to choose a liquid with a surface tension that varies considerably with temperature (high β) and has a low thermal conductivity and viscosity. The role of the low thermal conductivity is to reduce the heat load required to maintain the desired temperature difference between ridges, while a large β and small μ lead to larger thermocapillary stresses and pumping velocities, respectively.

For an illustrative calculation, we assume that the liquid is water and the average background temperature is 20°C. For this combination, the surface tensions coefficient $\beta \approx 1.5 \times 10^{-4} \text{ N K}^{-1}$, the viscosity $\mu \approx 0.9 \times 10^{-3} \text{ kg m}^{-1}\text{s}^{-1}$ and the thermal conductivity $k = 0.606 \text{ W m}^{-1}\text{K}^{-1}$ (Linstorm 1998). Now, if we choose our device parameters to be $\Delta T^* = 1 \text{ K}$, $H^* = 50 \text{ }\mu\text{m}$, $\epsilon = 1$, $\eta = 0.025$ and $\delta = 0.025$, we predict the maximum output power per wall area to be $0.13 \times 10^{-6} \text{ W cm}^{-2}$. This was calculated by evaluating P^* and converting into a per square centimetre value. Similarly, the total thermal power required to set up the temperature field can be determined from Q^* , which for the situation considered above, is 0.47 W cm^{-2} resulting in an efficiency $E = 2.87 \times 10^{-7}$. Irrespective of this low value of efficiency, the magnitude of thermal power required is not large and this mechanism could reasonably use waste heat to provide useful mechanical power to small-scale electromechanical systems, e.g. storing energy in some form, such as a spring, for use at a later time. In the future, devices could be designed that utilise the small microfluidic length scales to pack numerous devices into a compact, composite device that provides more power conversion. However, the present work has demonstrated the possibility to convert thermal power to mechanical power through thermocapillary stresses at fluid interfaces.

The device set-up considered here, with the various simplifications required for theoretical analysis, is not without its practical limitations. On the modelling side the assumption of small Re and Pe will break down at large pumping velocities. Even in the example above, $Re \approx 9$ and $Pe \approx 50$. However, although the effect of non-zero Re has not been studied, Crowdy *et al.* (2023) investigated the effect of Pe on U_{pump} and found that, for $Pe \approx 50$, the pumping velocity U_{pump} was still around 70 % of the value when $Pe = 0$. And finally, among other challenges, there may be practical issues in the design of such a device due to difficulties in microfluidic fabrication; however, the annular set-up depicted in figure 1(a) could be accomplished via a design like a cup-and-bob rotational viscometer, which may simplify fabrication.

Supplementary material. Supplementary material is available at <https://doi.org/10.1017/jfm.2025.188>.

Funding. M.D.M. and D.C. were supported by CBET-EPSC Grant EP/V062298/1. T.L.K. was supported by a Chapman Fellowship in the Department of Mathematics, Imperial College London. M.H. was supported through NSF Award No. 2140033.

Declaration of interests. The authors report no conflict of interest.

REFERENCES

- AJDARI, A. 2000 Pumping liquids using asymmetric electrode arrays. *Phys. Rev. E* **61** (1), R45–R48.
- AMADOR, G.J., REN, Z., TABAK, A.F., ALAPAN, Y., YASA, O. & SITTI, M. 2019 Temperature gradients drive bulk flow within microchannel lined by fluid-fluid interfaces. *Small* **15** (21), 1900472.
- BAIER, T., STEFFES, C. & HARDT, S. 2010a Numerical Modelling Of Thermocapillary Flow On Superhydrophobic Surface, In *14th International Conference on Miniaturized Systems for Chemistry and Life Sciences, number October*, pp. 1799–1801.

- BAIER, T., STEFFES, C. & HARDT, S. 2010*b* Thermocapillary flow on superhydrophobic surfaces. *Phys. Rev. E* **82** (3), 037301.
- CROWDY, D.G. 2011 Frictional slip lengths for unidirectional superhydrophobic grooved surfaces. *Phys. Fluids* **23** (7), 072001.
- CROWDY, D.G. 2020 *Solving Problems in Multiply Connected Domains*. Society for Industrial and Applied Mathematics.
- CROWDY, D.G., MAYER, M.D. & HODES, M. 2023 Asymmetric thermocapillarity-based pump: concept and exactly solved model. *Phys. Rev. Fluids* **8**, 094201.
- GAME, S.E., HODES, M. & PAPAGEORGIOU, D.T. 2019 Effects of slowly varying meniscus curvature on internal flows in the Cassie state. *J. Fluid Mech.* **872**, 272–307.
- HODES, M., KIRK, T.L., KARAMANIS, G. & MACLACHLAN, S. 2017 Effect of thermocapillary stress on slip length for a channel textured with parallel ridges. *J. Fluid Mech.* **814**, 301–324.
- HODES, M., KANE, D., BAZANT, M.Z. & KIRK, T.L. 2023 Asymptotic Nusselt numbers for internal flow in the Cassie state. *J. Fluid Mech.* **977**, A18.
- LINSTORM, P. 1998 NIST chemistry webbook, NIST standard reference database number 69. *J. Phys. Chem. Ref. Data Monograph* **9**, 1–1951.
- MAYER, M.D., KADOKO, J. & HODES, M. 2021 Two-dimensional numerical analysis of gas diffusion-induced Cassie to Wenzel state transition. *J. Heat Transfer* **143** (10), ISSN0022–1481.
- PHILIP, J.R. 1972*a* Flows satisfying mixed no-slip and no-shear conditions. *J. Appl. Maths Physic* **23** (6), 960–968.
- PHILIP, J.R. 1972*b* Integral properties of flows satisfying mixed no-slip and no-shear conditions. *J. Appl. Maths Physic* **23** (6), 960–968.
- TOMLINSON, S.D., MAYER, M.D., KIRK, T.L., HODES, M. & PAPAGEORGIOU, D.T. 2024 Thermal resistance of heated superhydrophobic channels with thermocapillary stress. *ASME J. Heat Mass Transfer* **146** (2), 1-28328469–28328414.
- TREFETHEN, L.N. 2000 Spectral methods in MATLAB. In *Spectral Methods in MATLAB*. Society for Industrial and Applied Mathematics.